ACS APPLIED MATERIALS & INTERFACES

www.acsami.org Research Article

Solution Blowing Synthesis of Li-Conductive Ceramic Nanofibers

Zhennan Huang, Alexander Kolbasov, Yifei Yuan, Meng Cheng, Yunjie Xu, Ramin Rojaee, Ramasubramonian Deivanayagam, Tara Foroozan, Yuzi Liu, Khalil Amine, Jun Lu, Alexander L. Yarin,* and Reza Shahbazian-Yassar*

Cite This: *ACS Appl. Mater. Interfaces* 2020, 12, 16200–16208 Read Online

ACCESS | Metrics & More | Article Recommendations | Supporting Information

ABSTRACT: Solid state electrolytes (SSEs) offer great potential to enable high-performance and safe lithium (Li) batteries. However, the scale-up synthesis and processing of SSEs is a major challenge. In this work, three-dimensional networks of lithium lanthanum titanite (LLTO) nanofibers are produced through a scale-up technique based on solution blowing. Compared with the conventional electrospinning method, the solution blowing technique enables high-speed fabrication of SSEs (e.g., 15 times faster) with superior productivity and quality. Additionally, the room-temperature ionic conductivity of composite polymer electrolytes (CPEs) formed from solution-blown LLTO fibers is 70% higher than the ones formed from electrospun fibers (1.9×10^{-4} vs 1.1×10^{-4} S cm^{-1} for 10 wt % LLTO fibers). Furthermore, the cyclability of the CPEs made from solution-blown fibers in the symmetric Li cell is more than 2.5 times that of the CPEs made from electrospun fibers. These comparisons show that solution-blown ion-conductive fibers hold great promise for applications in Li metal batteries.

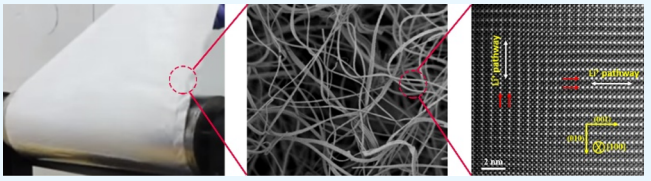

KEYWORDS: *solution blowing, solid state nanofibers, mass production, Li-ion conductivity, Li metal batteries*

INTRODUCTION

With the trend of developing battery technology toward high energy density, the concern on the safety issues arises. Thus, considerable research has focused on replacing the flammable liquid electrolytes with solid electrolytes in current rechargeable lithium-ion batteries. To date, numerous solid state electrolytes (SSEs) have been developed, including organic polymers,[1−4] inorganic sulfides,[5−8] oxides,[9−11] and others.[12−14] Among all these electrolytes, oxide-based solid electrolytes have attracted significant interest due to the following advantages. First, oxide solid electrolytes have relatively high Li-ion conductivity (>10^{-4} S cm^{-1}) at room temperature (RT).[15] Second, their wide electrochemical stability window[11] allows the presence of high battery voltage for high energy output. More importantly, oxide-based electrolytes possess high stiffness to prevent Li dendrite growth,[16,17] which significantly alleviates the safety concern in batteries, even with Li metal anodes. Last but not the least, the nonflammability and high stability at wide range of temperatures allow the batteries to be applicable for operation in complicated environments.

Conventionally, ceramic SSEs are produced via the solid-state reaction method,[18−20] which is simple. However, this approach demands huge energy consumption in the form of repeated long-time processing and high-temperature calcinations.[21,22] In addition, coarse grains[22] and impurities caused by the huge Li loss at high temperatures[22−24] always cause performance degradation. Wet chemical processes (e.g., hydrothermal[25,26] and sol−gel[27−30]) are also common approaches to achieve ceramic SSEs with better control of chemical composition and morphology.[26,31] However, the issues with prolonged treatments[27,32] still exist, and the yield (depending on the size of reactors) is even lower than that from solid-state reactions.[33] Some other approaches such as physical or chemical deposition[34,35] and electrospinning[1,36,37] have been reported to form good processability of ceramic SSE. However, the feasibility for mass production of these methods is limited.

Solution blowing is a novel method appropriate for scale-up production of nanofibers.[38−46] It is significantly faster than electrospinning[42] and, in distinction from the latter, the formation of fibers is derived aerodynamically rather than electrically. In this work, the solution blowing technique is utilized to produce ceramic nanofiber-based SSEs for the first time. A typical perovskite-type SSE lithium lanthanum titanite ($Li_{0.33}La_{0.557}TiO_3$ (LLTO)) was chosen as a target SSE material considering its reported high ionic conductivity.[15] The solution blowing parameters for fiber mat has been studied to guide the future works. The received ceramic fiber

Received: November 6, 2019
Accepted: February 26, 2020
Published: February 26, 2020

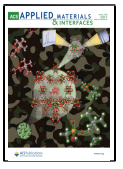

https://dx.doi.org/10.1021/acsami.9b19851
ACS Appl. Mater. Interfaces 2020, 12, 16200−16208

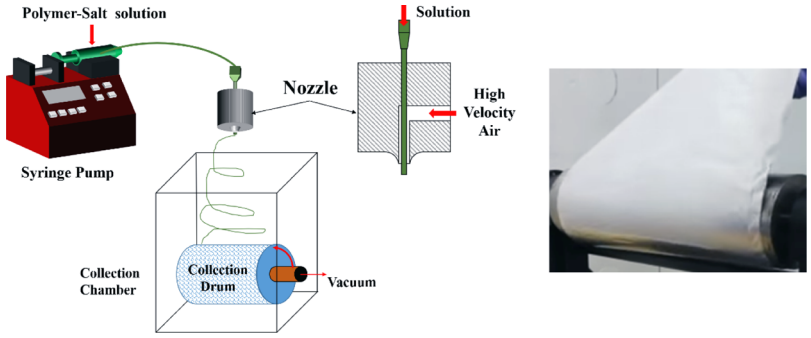

Figure 1. Schematic of solution blowing setup used to form nanofiber mat (left) and the collected large quantity fiber mat on the collection drum (right).

mat after calcination was investigated by X-ray diffraction (XRD) and scanning transmission electron microscopy (STEM) to demonstrate the crystallinity and atomic structure of nanofibers. The ceramic fibers were later mixed with poly(vinylidene fluoride-hexafluoropropylene) (PVDF-*co*-HFP) polymer to form a composite polymer electrolyte (CPE). The LLTO fiber-enhanced CPE membrane shows good thermal stability, high ion conductivity, as well as extremely long cycle life against Li metal with relatively low overpotential. The mechanism of enhanced thermal and electrochemical performance was determined, and it was proposed for the first time that the three-dimensional (3D) fiber network structures could not only maintain the structural stability of CPE at high temperatures but also create additional Li-ion pathways in CPE for improved ionic conductivity.

RESULTS AND DISCUSSION

The LLTO-containing nanofibers for use in the solid electrolyte were fabricated by means of solution blowing, and the schematic of the setup is shown in Figure 1 (an image of the setup is also shown in Figure S1). In short, an 18 gauge needle was inserted concentrically into a nozzle, placing it in the middle of a high velocity air jet (of the order of 200 m/s) with a gas pressure of 45 psi. The polymer solution with salt was then fed through the needle by a syringe pump. The solution jets were vigorously stretched and bent by the surrounding air jet. This fiber forming process was captured by an ultrafast camera as shown in Movie S1. Finally, as the solvent evaporated, solid fibers were collected on a wire mesh, with suction applied to the bottom of the collector for proper fiber retention. A small room heater was used during this process to elevate the ambient air temperature and increase the evaporation rate in the fibers.

Viscoelasticity of the polymer solution is the key parameter to make sure that the prepared solution has a continuous spinnability. This parameter is characterized by the relaxation time. An in-house elongation viscometer[41,47] was used to measure characteristic relaxation time of the 10 wt % polyvinylpyrrolidone (PVP) in dimethylformamide (DMF) solutions with and without salt. In addition, to reveal the effect of salt concentration on the viscoelasticity of the polymer solutions, three different amounts of salt precursors (0.4617, 0.9233, and 1.8466 g) were added to PVP solutions to form mixtures. The prepared four solutions were denoted as SOLN-1, SOLN-2, SOLN-3, and SOLN-4, in the exact order of the increased salt amount, where SOLN-1 is pure PVP solution (no salt) and SOLN-4 contains the largest amount of total salt precursors (Table S1). The thinning of the cross-sectional diameter at the center of SOLN-1 solution thread was captured by a high-speed camera (schematic shown in Figure 2a) and

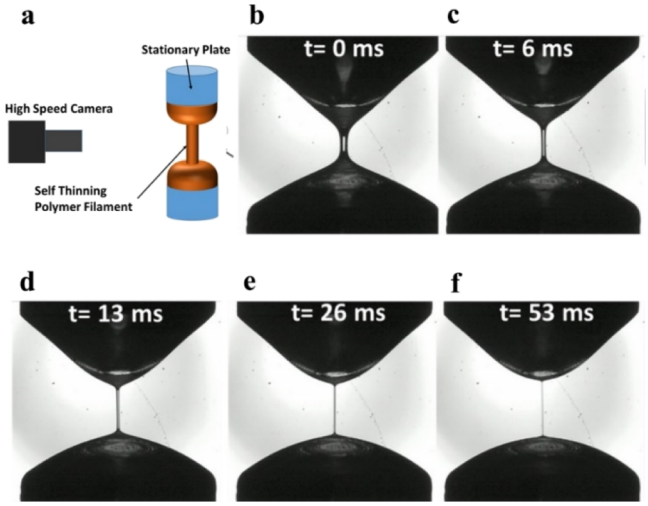

Figure 2. Viscoelastic thread thinning of the prepared solution. (a) Schematic of the setup with a high-speed camera. (b–f) series of time lapse images taken by a digital camera, showing a self-thinning thread of polymer solution.

used to elucidate the relaxation time (Figure 2b–f). Shear viscosity was also measured and is presented in Figure S2. PVP typically exhibits viscoelastic behavior and possesses elongational viscosity (i.e., reveals significant viscoelastic effects in strong uniaxial stretching, e.g., spinnability in fiber forming). In simple shear testing of PVP, the shear-thinning (also a viscoelastic manifestation) was not observed, most probably because it happened at lower shear rates (beyond the measurement capability of our shear viscometer). On the other hand, when LLTO salt precursors are added, it is likely that they make complexes with polymer macromolecules, creating a physical network. This can shift shear-thinning to higher shear rates where it could be measured.

The relaxation time of a pure 10 wt % PVP solution, as well as of the three different solutions containing salt, affects the diameter, d thinning in time, t according to the following equation

$$d = d_0 \exp\left(-\frac{t}{3\theta}\right) \quad (1)$$

where d_0 is the initial value at $t = 0$, and θ is the viscoelastic relaxation time. The measurement results used for evaluation

https://dx.doi.org/10.1021/acsami.9b19851
ACS Appl. Mater. Interfaces 2020, 12, 16200–16208

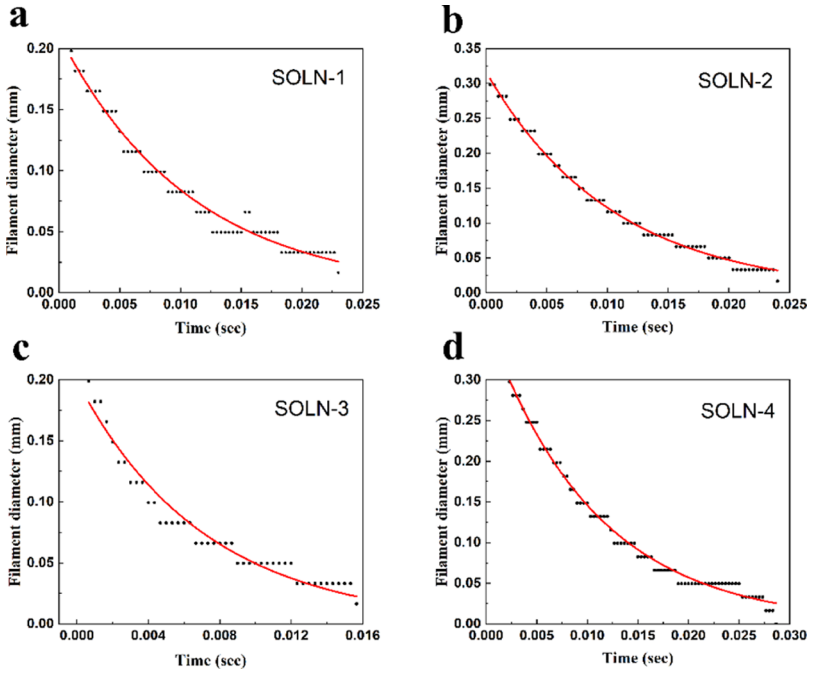

Figure 3. Elongation viscometer test as an indication of spinnability showing the thread diameter as a function of time for (a−d) SOLN-1 to SOLN-4. The experimental data are shown by symbols, whereas eq 1 is represented by solid red lines.

of θ are shown in Figure 3. The relaxation times for these four solutions are found as 3.56, 3.54, 2.40, and 3.45 ms, respectively (Figure 3a−d). This indicates that the salt does not affect the viscoelasticity of the PVP solutions and does not diminish their spinnability, which is important for nanofiber forming. The presence of salt ions in the polymer solution affects polymer solubility in the interplay with the isoelectric point. Accordingly, the salt concentration and the uncontrollable impurities present in the solvent in the interplay with the isoelectric point most probably diminish solubility in the case of SOLN-3, which results in its lower relaxation time.

The targeted LLTO nanofibers were obtained by calcinating the as-blown fiber mat at 850 °C in air with the ramp rate of 10 °C/min and keeping at 850 °C for 2 h. The large specimen of a fiber mat before and after calcination is shown in Figure S3. The fiber morphology was further studied by field-emission scanning electron microscopy (SEM). Figure 4a,b depicts nanofibers formed using solution blowing before and after calcination. The corresponding size distributions were analyzed and are shown as insets in the figures. It should be noted that the mean diameter of the fibers shrinks after calcination, which is the result of the removal of the polymer during high-temperature treatment. The close-up images of solution-blown fibers made from SOLN-3 and SOLN-4 are shown in Figure 4c,d, Large area LLTO fiber morphology was also identified through SEM, as shown in Figure S4, which reveals good fiber quality. The fibers both present certain kind of porous structure, which is caused by the removal of the polymer as well. As expected, as SOLN-3 contains only half of the salt amount in comparison to SOLN-4, the fibers made from SOLN-3 are more porous than the ones from SOLN-4. In comparison, pure PVP solutions were also used for solution blowing and the detailed analysis is shown in Figure S5a−c. Additionally, the traditional fiber-forming method—electrospinning (schematically shown in Figure S6) has been used as

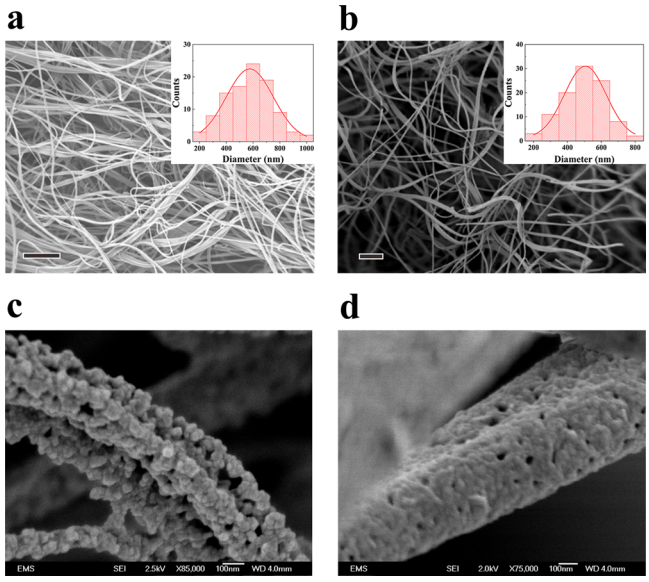

Figure 4. SEM images of solution-blown nanofiber networks. (a,b) SEM images of the as-spun nanofibers and nanofibers after calcination; scale bar is 10 μm. Inset shows the corresponding size distribution of nanofibers. (c,d) SEM images show single fiber morphology resulting from SOLN-3 and SOLN-4.

well, and the corresponding fiber morphology and size distribution are shown in Figure S5d−f.

The detailed analysis is quantified in Table S2, where the fiber diameters obtained using either solution blowing or electrospinning are listed. The data for the calcined solution-blown fibers was also added. The mean diameter of fibers is in the 500−600 nm range, which means that the sizes of the fibers formed by solution blowing and electrospinning are mainly the same. The diameter of the solution-blown fibers with or without salt is also close, within ∼6% difference ((577−544)/577 = 5.7%), which means that the salt effect is

https://dx.doi.org/10.1021/acsami.9b19851
ACS Appl. Mater. Interfaces 2020, 12, 16200−16208

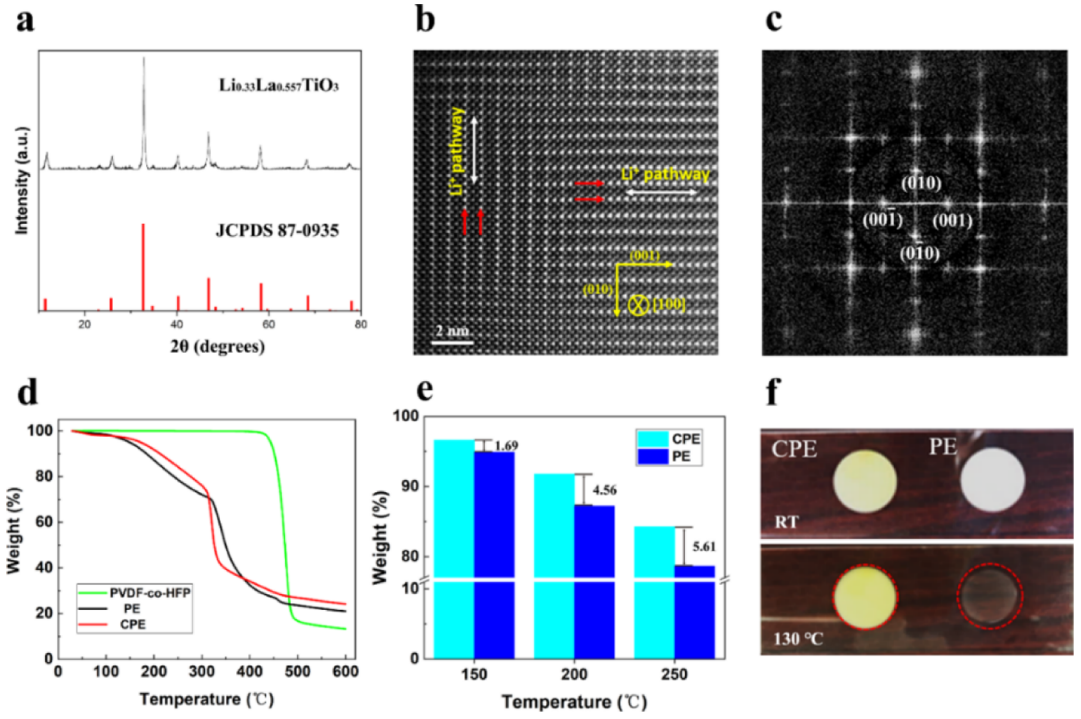

Figure 5. Phase structure characterization of the prepared LLTO nanofibers and thermal stability test of the CPE. (a) XRD pattern of the ceramic fibers. (b) Atomic STEM−HAADF image of LLTO at [100] zone axis. (c) FFT analysis of the atomic HAADF image showing a single crystal structure. (d) TGA curves of PVDF-*co*-HFP, PE, and CPE. (e) Weight difference of CPE and PE from TGA curves in figure (d). (f) Images showing the heating behavior of CPE and PE on a hot plate at 130 °C for 15 min.

limited. In solution blowing, the flow rate was 6 mL/h, whereas in electrospinning, the flow rate of only 0.4 mL/h could be achieved for a single needle. Accordingly, the solution blowing process was 15 (6 vs 0.4 mL/h) times faster than the electrospinning method. Additionally, in the case of solution blowing, it is easy to stack multiple needles close to each other and increase production rate by another 1 or 2 orders of magnitude (Figure S7). This type of upscaling is hardly possible with electrospinning due to the electrical repulsion between the polymer jets, which causes the laydown nonuniformities. Thus, by using the scaled-up solution blowing setup (multiple nozzle blowing nanofibers simultaneously, as shown in Figure S8. Reproduced from a previous work[42]), liter-level solution is easily consumed to form nanofibers, indicating its ultrafast productivity. The electrospun LLTO (E-LLTO) fibers also have porous structure, which is visualized through transmission electron microscopy (TEM) imaging. As show in Figure S9, the low magnification TEM image reveals a porous structure (Figure S9a). Detailed surface structure can be found from the STEM image (Figure S9b), in which some pores can be clearly seen (marked as blue arrows). Further study is needed to reduce the porosity of LLTO fibers for better electrochemical performance.

The solution blowing technique shows promising results as a scale-up production method. The quality of the synthesized solution-blown LLTO (S-LLTO) fibers was further examined by XRD. All main peaks (Figure 5a) correspond to LLTO (JCPDS 87-0935), indicating the successful preparation of LLTO nanofibers. The crystal structures of the fibers were also determined by atomic scale high-angle annular dark-field (HAADF)−STEM analysis. As shown in Figure 5b, the *d*-spacing of the two vertically aligned planes are measured to be 3.84 Å, corresponding to the {100} planes of LLTO along [100] zone axis. Nanosized domains always existed in LLTO, which is formed by the alternation of La-rich and La-poor sites and have an effect on Li^+ conductivity.[48,49] In the HAADF image of Figure 5b, the atom intensity is proportional to the average atomic number in that column.[50] Thus, the La-rich and La-poor areas can be easily identified. In the atomic scale STEM image, La-poor areas (marked with white two-way arrows) showing much darker contrasts than La-rich areas (marked with red arrows). Typically, La-poor areas act as Li-ion pathways and La-rich areas act as walls for the pathways as indicated in the image. The corresponding fast Fourier transform (FFT) analysis (Figure 5c) of the atomic image shows a single crystal structure, which means that LLTO domain structures are not polycrystalline. With the analysis of XRD together with atomic-scale STEM, the synthesis of high-purity LLTO through solution blowing is confirmed.

The S-LLTO nanofibers were then composited with PVDF-*co*-HFP polymer to become 3D fiber network-enhanced CPE because PVDF-*co*-HFP-based solid polymer electrolyte (SPE) exhibits good mechanical stability and high ionic conductivity,[52] and ceramic fibers have been recently reported to be excellent additives to improve the electrochemical performance of polymer electrolyte to the next level.[36] Thermal stability is a crucial performance requirement of polymer-based electrolytes and was investigated here. As presented in the thermogravimetric analysis (TGA) curves in Figure 5d, the thermal degradation of pure PVDF-*co*-HFP is about 430 °C and the thermal stability decreased after adding Li salt (LiTFSI) and LLTO nanofibers. Just right before 100 °C, there is a minor weight loss of the SPE and CPE, which is due to the trapped moisture in the electrolyte. Notably, the CPE exhibits much better thermal stability than the SPE before 300 °C, as shown by the relatively mild weight loss curve (red) compared to the

https://dx.doi.org/10.1021/acsami.9b19851
ACS Appl. Mater. Interfaces 2020, 12, 16200−16208

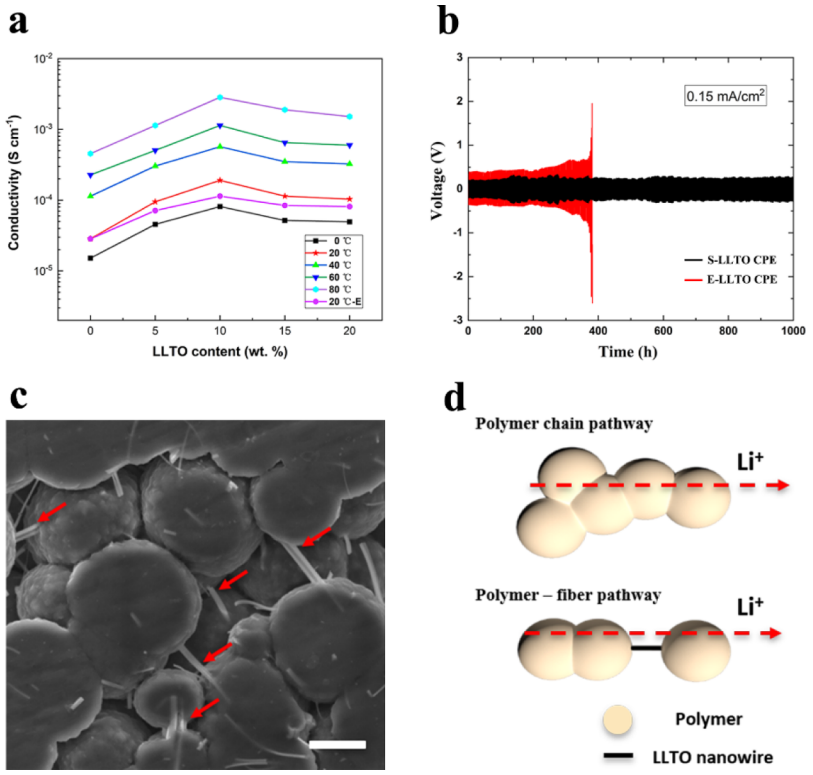

Figure 6. Electrochemical test of the prepared CPE and Li-ion conductive pathways in CPE. (a) Ionic conductivity of CPE as a function of S-LLTO fiber concentrations at various temperatures. The data for ionic conductivity of E-LLTO fiber concentrations at RT (named as 20 °C-E) is also shown for comparison. (b) Cycling performance of symmetric Li cells with 10 wt % S-LLTO and E-LLTO fibers added to CPE. (c) SEM image of the synthesized CPE (10 wt % S-LLTO adding); scale bar is 5 μm. (d) Schematic of the Li-ion diffusion pathways in CPE.

steeper black curve. The different temperature points in this range were further analyzed. As shown in Figure 5e, at 150 °C, the weight difference of CPE and PE is 1.69%, with the temperature increase, the difference expands to 4.56 and 5.61% at 200 and 250 °C, respectively. These observations indicate that the addition of ceramic fibers may form strong bonding with the surrounding polymer chains to slow their degradation. There is rapid decomposition of the CPE that starts at around 310 °C, where the bonding between the polymers and nanofibers breaks, indicating that this bonding is strong enough at a wide range of temperatures (up to ~300 °C).

Another thermal stability evaluation was conducted by heating the developed CPE and SPE at 130 °C on a hot plate for 15 min. Figure 5f shows the images of the CPE and PE membranes at RT and after 130 °C heat treatment. As it can be seen in Figure 5e, the PE shows an obvious shrinkage and melting at this temperature as compared with the status at RT, whereas the fiber-enhanced CPE remains almost intact upon exposure to the heat. Therefore, the CPE shows much better shape stability at high temperatures with the help of fiber networks. As a result, the 3D LLTO fiber network-reinforced polymer electrolyte would slow down the short circuit caused by the shrinkage of the polymer membrane electrolyte at high temperatures and the following disastrous electrodes contact.

To realize the ionic conductivity of the synthesized S-LLTO fibers, a LLTO pellet was prepared by cold pressing (Figure S10a,b) followed by 4 h calcination at 800 °C. The ionic conductivity of the pellet was tested to be 6.10×10^{-5} S cm^{-1} (Figure S10c). The ionic conductivity of the CPE with a series of ceramic fiber content (0–20 wt % of the total weight of PVDF-*co*-HFP and LiTFSI), at different temperatures (from 0 to 80 °C) was measured and the results are shown in Figure 6a. With the increasing amount of ceramic fibers, the ionic conductivity of CPE increases and reaches to the peak with the addition of 10 wt.% nanofibers and then slightly decreases. The highest conductivity is about 1.90×10^{-4} S cm^{-1} at RT, which is an order of magnitude higher than the performance of PE (2.80×10^{-5} S cm^{-1}). It is worth noting that, there is more than 70% improvement in ionic conductivity compared with the CPE made from 10 wt % E-LLTO fibers at RT (1.10×10^{-4} S cm^{-1}, shown with purple symbols in Figure 6a), which is elaborated later. The conductivity starts to drop from 15 wt %, which may be owing to the aggregation of nanofibers at high concentrations. Therefore, the cycling performance was measured in a symmetric Li−CPE−Li cell by using the 10 wt % LLTO CPE. Figure 6b shows the voltage profile of the continued Li plating and striping cycling with a current density of 0.15 mA/cm^2 at 25 °C. The overpotential of the CPE resulting from E-LLTO fibers was around 0.4 V initially, but gradually increased over 200 cycles and failed at 382 cycles. Whereas the overall overpotential with the CPE resulting from S-LLTO fibers was stable around 0.3 V for up to 1000 cycles (see the enlarged view of some cycles in Figure S11, interfacial engineering is needed in future works to reduce overpotential), indicating the promising application of the S-LLTO fibers in Li metal batteries.

To investigate the reasons behind the improvements from PE to CPE, the SEM characterization was used to visualize the structure of CPE with 10 wt % S-LLTO fibers. As shown in Figure 6c (the corresponding zoomed-in image and large area composite structure is shown as Figure S12.), the CPE shows well-dispersed LLTO nanofibers in porous polymer sphere

https://dx.doi.org/10.1021/acsami.9b19851
ACS Appl. Mater. Interfaces 2020, 12, 16200−16208

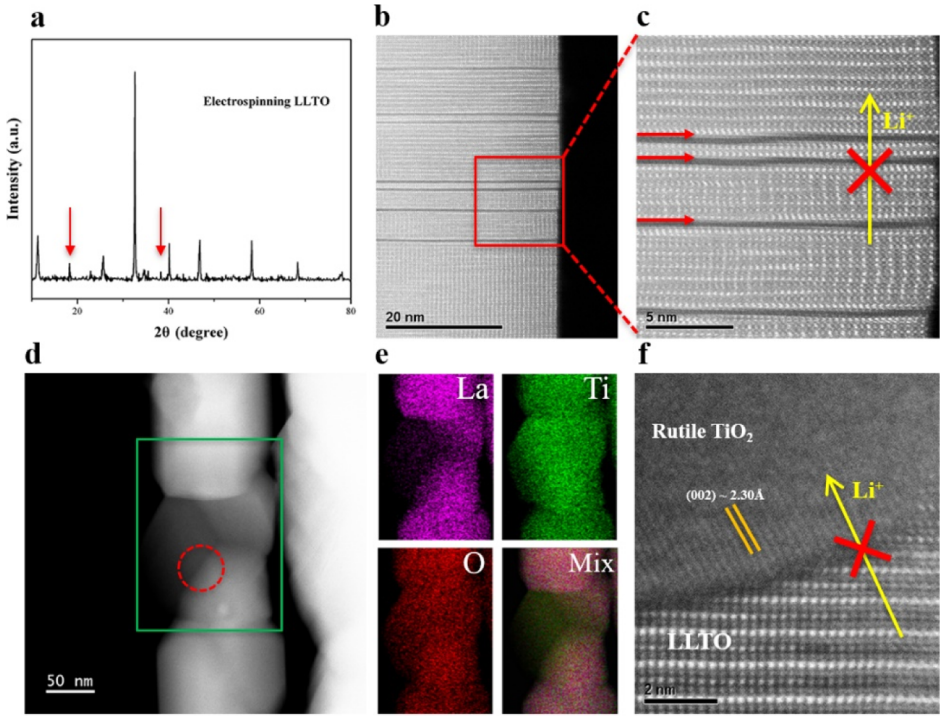

Figure 7. XRD and STEM analysis of electrospinning LLTO nanofibers. (a) XRD pattern of electrospinning LLTO nanofibers with certain kind of impurities (some of the irrelevant peaks pointed by red arrows). (b,c) Atomic STEM images showing ravine-like defective structures (atom columns missing, pointed by red arrows) from electrospun LLTO fibers, and an indication of Li-ion transport barrier. (d) HAADF−STEM image of grain boundary formed by LLTO and La_xTi_yO impurity. (e) EDS mapping of the green rectangular area in (d) showing La_xTi_yO (Ti rich) impurity. (f) Atomic STEM image showing the boundary [dashed circle range in (d)] of LLTO and Ti rich oxide, and an indication of Li-ion transport barrier.

structures. This kind of porous structure is common in PVDF-*co*-HFP-based polymer electrolytes[2,51] and is beneficial to soak organic liquid electrolyte to enhance the Li-ion conductivity. Interestingly, in our liquid-free CPE, the imbedded fibers were able to connect the adjacent separate polymer spheres as marked with the red arrows in the image. These connections could act as additional pathways for the transport of Li ions (schematically shown in Figure 6d), resulting in excellent electrochemical performance. In addition, LLTO nanoparticles are also synthesized through ball milling of the S-LLTO fibers (Figure S13a) to prepare LLTO particle CPE (P-CPE). From the SEM image of P-CPE (Figure S13b), the nanoparticles are well dispersed in polymers and the CPE shows a porous structure as we mentioned previously. However, in contrast with the fiber-based CPE (Figure 6c), the adjacent separate polymer spheres are not connected by the nanoparticles. Better connectivity between the adjacent polymer spheres suggests that the fibrous structure of LLTO offers additional pathways for Li-ion transport. As a result, the P-CPE shows an ionic conductivity of 0.97×10^{-4} S cm^{-1} (Figure S14), which is well below the ionic conductivity of S-CPE. Also, as E-CPE contains impurities and defects that hinder the Li-ion transport along the fibers, the conductivity improvement from P-CPE is limited. These comparisons confirm the importance of fiber structures for Li-ion battery application. From the electrochemical stability window (Figure S15), the CPE was stable up to ~4.7 V, which is good to run most of the common cathode materials. The Li transference number (t_+) was found to be 0.23 (Figure S16), based on the following equation

$$t_+ = \frac{I_{ss}(\Delta V - I_0R_0)}{I_0(\Delta V - I_{ss}R_{ss})}$$

where I_0 and I_{ss} are the initial current and steady-state current, ΔV is the activation voltage, R_0 and R_{ss} are the initial and steady-state resistance, respectively. Finally, as the CPE has good ionic conductivity (~10^{-3} S cm^{-1}) at 60 °C, the LFP−S-CPE−Li cell is cycled at 60 °C, which shows good cyclability with specific capacity ~135 mA h/g and more than 98% coulombic efficiency (Figure S17).

Considering that the polymer matrix was the same for both the electrospun and solution-blown fibers, we studied the microstructure of E-LLTO fibers to further understand the improvements in the electrochemical performance of the CPEs made from E-LLTO to S-LLTO. It appears that the E-LLTO nanofibers suffer from impurities and significant structural defects. As evident in Figure 7, the LLTO nanofibers made from electrospinning show extra XRD peaks (Figure 7a, some of them are marked by red arrows) and could be correlated to La_xTi_yO secondary phases. This can be explained by the effect of the electric field applied during electrospinning that causes the migration of the salt ions to the free surface.[52] More specifically, the impurities and defects are caused by the electrically driven ion migration to the jet surface in electrospinning in distinction from solution blowing, which does not involve any electric field. The La^{3+} and Ti^{4+} ions originate from the salt dissociation in the polymer DMF solution. The charge relaxation time, $\tau_C = \varepsilon/4\pi\sigma$ (in CGS units), where ε and σ are the dielectric permittivity and conductivity of liquid, respectively. The charge relaxation time, τ_C is in the 1 μs to 1 ms range.[41] In electrospinning, polymer

https://dx.doi.org/10.1021/acsami.9b19851
ACS Appl. Mater. Interfaces 2020, 12, 16200−16208

jet velocities are on the scale of U = 1 m/s, which means that in such jets, all ions will have a trend to move to the free surface at the jet length well below $U\tau_C$ = 1 mm, that is, practically at the jet origin. This estimate is corroborated by detailed electrokinetic simulations.[52] Accordingly, ion redistribution to the jet surface in electrospinning happens practically immediately, and the electrospun nanofibers are highly segregated regarding La^{3+} and Ti^{4+}. This nonuniform distribution causes the impurities and defects in the E-LLTO fibers (Figure 7). On the other hand, there is no electrically driven ion migration in solution-blown jets, which results in solution-blown nanofibers with high-phase purity. In addition, a deeper understanding was also achieved through atomic scale HAADF−STEM analysis on E-LLTO fibers. As presented in Figure 7b, plenty of structural defects (ravine structures, pointed by the red arrows) were observed in the E-LLTO grains. The high magnification view of the defective region (Figure 7c) shows clearly the missing atom columns, which are evidences of local salt deficiency caused by the salt migration during electrospinning under the high electric field. These can become structural barriers for the diffusion of Li ions inside the LLTO grains. The regions indicating local salt accumulation on electrospun fibers was also revealed by HAADF imaging (Figure 7d) and energy-dispersive system (EDS) mapping (Figure 7e, green rectangular region in Figure 7d). These images show a Ti-rich grain (minor La signals) between LLTO grains and can be indexed to the rutile TiO_2 phase through d spacing analysis at the grain boundary area (Figure 7f, corresponding to the dashed circled region in Figure 7d). The secondary phases can be barriers for Li ion to transport as well. Thus, both in-grain ravine defects and out-of-grain secondary phases can prevent the facile movement of Li ions, resulting in the poor performances compared to solution blowing fibers.

As a proof of the applicability of the solution blowing technique to other ceramic electrolytes, another popular SSE-$Li_7La_3Zr_2O_{12}$ has also been fabricated. The fiber structure is revealed by a SEM image (Figure S18a), and the quality is determined by XRD (Figure S18b), showing high purity cubic structures. Thus, the high feasibility of the solution blowing method in fabricating ceramic electrolytes is confirmed.

CONCLUSIONS

In summary, ceramic SSE nanofibers were successfully fabricated through solution blowing technique for the first time. This fabrication method has approximately 15 times higher production rate compared with the traditional electrospinning method under the same conditions and holds great promise for scale-up processing. In comparison to electrospun nanofibers, the solution-blown nanofibers reveal an intact atomic structure and a higher phase purity. Owing to these advantages, the RT ionic conductivity of the CPE made from solution-blown LLTO 3D fiber networks is more than 70% higher than that of the CPE made from E-LLTO fibers (1.9×10^{-4} vs 1.1×10^{-4} S cm^{-1}) and the cycling life against Li metal is almost tripled. The improvements on thermal stability and electrochemical performance from PE to fiber-enhanced CPE are ascribed to the 3D solution-blown LLTO fiber skeleton for not only maintaining the polymer structure at high temperature but also acting as additional Li-ion pathways in CPE. Our work opens a new direction to scale-up processing of SSEs for safe and viable lithium batteries. The findings also provide new understanding on the thermal-electrical improvement of the fiber-enhanced composite solid electrolytes.

EXPERIMENTAL SECTION

Preparation of Precursor Solutions. The solutions used for blowing were a mixture of a polymer solution and a salt precursor solution. The polymer solution was made by dissolving 10 wt % PVP (molecular weight 1,300,000; Sigma-Aldrich) in DMF. The salt solution was prepared by dissolving certain amount of salt precursors—0.0816 g of $LiNO_3$ (99%; Alfa Aesar, 20% more $LiNO_3$ is used to compensate the Li loss during calcination), 0.8050 g of $La(NO_3)_3{\cdot}6H_2O$ (99.9%; Alfa Aesar), and 0.96 g of titanium isopropoxide (97%; Sigma-Aldrich) in DMF. Additionally, 15 vol % of acetic acid was added to the salt solution to avoid hydrolysis. The polymer solution and salt solution were then mixed under magnetic stirring for 3 h to form transparent and homogeneous spinning solution. Two more solutions were prepared by simply changing the salt precursor amount to 25 and 50 wt % of the aforementioned value.

Viscosity Test. The viscosity was measured in a simple shear flow using a Brookfield LV-II+ cone and plate viscometer. The measurements were done at multiple shear rates. Each shear rate was held for 30 s before taking a reading.

Preparation of LLTO Ceramic Fibers. The as-spun nanofiber mats were placed inside an aluminum oxide tray and calcined using a muffle furnace to oxidize them and achieve a ceramic metal-oxide structure.

Preparation of CPE. The CPE was then prepared first by dissolving PVDF-*co*-HFP and lithium bis(trifluoromethanesulfonyl)-imide (LiTFSI) in DMF solution. Subsequently, different amounts of LLTO fibers (5, 10, 15, and 20 wt %, respectively) were added into the solution to form a mixture. After stirring the mixtures at 80 °C for 5 h, the CPE was casted on a glass plate by a doctor blade and dried in vacuum at 80 °C overnight.

Parameters for Electrospinning Method. Fibers were also produced by electrospinning as a comparison. Electrospinning was conducted at RT. The collector was a rotating drum located at a distance of 15 cm from an 18 gauge needle (serving as a spinneret or a die). A syringe pump was used to supply continuously a salt/polymer solution to the spinneret at a flow rate of 0.4 mL/h. The electric field strength between the needle and collector was sustained at 0.67 kV/cm.

ASSOCIATED CONTENT

Supporting Information

The Supporting Information is available free of charge at https://pubs.acs.org/doi/10.1021/acsami.9b19851.

Digital photo of solution blowing setup; solution viscosity test; images of fiber mat before and after calcination; SEM images of solution-blown and electrospun fibers; schematic of electrospinning set-up; scale-up solution blowing setup; SEM and XRD characterization of LLZO fibers; precursor salt amount description; and fiber diameter analysis (PDF)

Fiber forming process (MP4)

AUTHOR INFORMATION

Corresponding Authors

Alexander L. Yarin − *Department of Mechanical and Industrial Engineering, University of Illinois at Chicago, Chicago, Illinois 60607, United States;* orcid.org/0000-0001-8032-2525; Email: ayarin@uic.edu

Reza Shahbazian-Yassar − *Department of Mechanical and Industrial Engineering, University of Illinois at Chicago, Chicago, Illinois 60607, United States;* orcid.org/0000-0002-7744-4780; Email: rsyassar@uic.edu

https://dx.doi.org/10.1021/acsami.9b19851
ACS Appl. Mater. Interfaces 2020, 12, 16200−16208

Authors

Zhennan Huang − *Department of Mechanical and Industrial Engineering, University of Illinois at Chicago, Chicago, Illinois 60607, United States*

Alexander Kolbasov − *Department of Mechanical and Industrial Engineering, University of Illinois at Chicago, Chicago, Illinois 60607, United States*

Yifei Yuan − *Department of Mechanical and Industrial Engineering, University of Illinois at Chicago, Chicago, Illinois 60607, United States; Chemical Sciences and Engineering Division, Argonne National Laboratory, Lemont, Illinois 60439, United States*

Meng Cheng − *Department of Mechanical and Industrial Engineering, University of Illinois at Chicago, Chicago, Illinois 60607, United States*

Yunjie Xu − *Department of Chemistry, Illinois Institute of Technology, Chicago, Illinois 60616, United States*

Ramin Rojaee − *Department of Mechanical and Industrial Engineering, University of Illinois at Chicago, Chicago, Illinois 60607, United States;* orcid.org/0000-0001-5787-1630

Ramasubramonian Deivanayagam − *Department of Mechanical and Industrial Engineering, University of Illinois at Chicago, Chicago, Illinois 60607, United States;* orcid.org/0000-0003-1367-009X

Tara Foroozan − *Department of Mechanical and Industrial Engineering, University of Illinois at Chicago, Chicago, Illinois 60607, United States;* orcid.org/0000-0003-1334-3048

Yuzi Liu − *Center for Nanoscale Materials, Argonne National Laboratory, Lemont, Illinois 60439, United States;* orcid.org/0000-0002-8733-1683

Khalil Amine − *Chemical Sciences and Engineering Division, Argonne National Laboratory, Lemont, Illinois 60439, United States;* orcid.org/0000-0001-9206-3719

Jun Lu − *Chemical Sciences and Engineering Division, Argonne National Laboratory, Lemont, Illinois 60439, United States;* orcid.org/0000-0003-0858-8577

Complete contact information is available at: https://pubs.acs.org/10.1021/acsami.9b19851

Author Contributions

Z.H. and A.K. contributed equally to this work. Z.H. conceived the idea with the direction of R.S.-Y. and A.L.Y. Z.H. and A.K. conducted the sample preparation. Y.Y. helped on TEM and battery analysis, R.D. helped on the electrochemical tests, Y.X. and T.F. performed the XRD and TGA. M.C., R.R., Y.L., K.A., and J.L. were involved in the discussion and provided necessary data analysis. All author discussed the manuscript and assisted in the revision.

Notes

The authors declare no competing financial interest.

■ ACKNOWLEDGMENTS

This project is financially supported by National Science Foundation (NSF) award no. CBET-1805938. This work made use of JOEL JEM-ARM 200CF in the Electron Microscopy Core of UIC's Research Resources Center. JOEL JEM-ARM 200CF is supported by an MRI-R2 grant from the National Science Foundation DMR-0959470. Y.L. acknowledges the use of the Center for Nanoscale Materials, an Office of Science user facility, supported by the U.S. Department of Energy, Office of Science, Office of Basic Energy Sciences, under Contract no. DE-AC02-06CH11357. Work at Argonne National Laboratory was supported by the U. S. Department of Energy (DOE), Office of Energy Efficiency and Renewable Energy, Vehicle Technologies Office. Argonne National Laboratory is operated for DOE Office of Science by UChicago Argonne, LLC, under contract number DE-AC02-06CH11357.

■ REFERENCES

(1) Liu, W.; Liu, N.; Sun, J.; Hsu, P.-C.; Li, Y.; Lee, H.-W.; Cui, Y. Ionic Conductivity Enhancement of Polymer Electrolytes with Ceramic Nanowire Fillers. *Nano Lett.* **2015**, *15*, 2740−2745.

(2) Cheng, M.; Jiang, Y.; Yao, W.; Yuan, Y.; Deivanayagam, R.; Foroozan, T.; Huang, Z.; Song, B.; Rojaee, R.; Shokuhfar, T.; Pan, J.; Shahbazian-Yassar, R. Elevated-Temperature 3D Printing of Hybrid Solid-State Electrolyte for Li-Ion Batteries. *Adv. Mater.* **2018**, *30*, 1800615.

(3) Mindemark, J.; Lacey, M. J.; Bowden, T.; Brandell, D. Beyond PEO—Alternative host materials for Li+-conducting solid polymer electrolytes. *Prog. Polym. Sci.* **2018**, *81*, 114−143.

(4) Zhao, Y.; Sun, X. Molecular Layer Deposition for Energy Conversion and Storage. *ACS Energy Lett.* **2018**, *3*, 899−914.

(5) Hood, Z. D.; Wang, H.; Pandian, A. S.; Peng, R.; Gilroy, K. D.; Chi, M.; Liang, C.; Xia, Y. Fabrication of Sub-Micrometer-Thick Solid Electrolyte Membranes of β-Li3 PS4 via Tiled Assembly of Nanoscale, Plate-Like Building Blocks. *Adv. Energy Mater.* **2018**, *8*, 1800014.

(6) Kamaya, N.; Homma, K.; Yamakawa, Y.; Hirayama, M.; Kanno, R.; Yonemura, M.; Kamiyama, T.; Kato, Y.; Hama, S.; Kawamoto, K. A lithium superionic conductor. *Nat. Mater.* **2011**, *10*, 682.

(7) Chang, D.; Oh, K.; Kim, S. J.; Kang, K. Super-Ionic Conduction in Solid-State $Li_7P_3S_{11}$-Type Sulfide Electrolytes. *Chem. Mater.* **2018**, *30*, 8764−8770.

(8) Kudu, Ö. U.; Famprikis, T.; Fleutot, B.; Braida, M.-D.; Le Mercier, T.; Islam, M. S.; Masquelier, C. A review of structural properties and synthesis methods of solid electrolyte materials in the Li_2S − P_2S_5 binary system. *J. Power Sources* **2018**, *407*, 31−43.

(9) Thangadurai, V.; Weppner, W. Recent progress in solid oxide and lithium ion conducting electrolytes research. *Ionics* **2006**, *12*, 81−92.

(10) Inaguma, Y.; Liquan, C.; Itoh, M.; Nakamura, T.; Uchida, T.; Ikuta, H.; Wakihara, M. High ionic conductivity in lithium lanthanum titanate. *Solid State Commun.* **1993**, *86*, 689−693.

(11) Thangadurai, V.; Narayanan, S.; Pinzaru, D. Garnet-type solid-state fast Li ion conductors for Li batteries: critical review. *Chem. Soc. Rev.* **2014**, *43*, 4714−4727.

(12) Maekawa, H.; Matsuo, M.; Takamura, H.; Ando, M.; Noda, Y.; Karahashi, T.; Orimo, S.-i. Halide-Stabilized LiBH4, a Room-Temperature Lithium Fast-Ion Conductor. *J. Am. Chem. Soc.* **2009**, *131*, 894−895.

(13) Manthiram, A.; Yu, X.; Wang, S. Lithium battery chemistries enabled by solid-state electrolytes. *Nat. Rev. Mater.* **2017**, *2*, 16103.

(14) Zhao, Y.; Liang, J.; Sun, Q.; Goncharova, L. V.; Wang, J.; Wang, C.; Adair, K. R.; Li, X.; Zhao, F.; Sun, Y.; Li, X. In situ formation of highly controllable and stable Na_3PS_4 as a protective layer for Na metal anode. *J. Mater. Chem. A* **2019**, *7*, 4119−4125.

(15) Stramare, S.; Thangadurai, V.; Weppner, W. Lithium Lanthanum Titanates: A Review. *Chem. Mater.* **2003**, *15*, 3974−3990.

(16) Khurana, R.; Schaefer, J. L.; Archer, L. A.; Coates, G. W. Suppression of Lithium Dendrite Growth Using Cross-Linked Polyethylene/Poly(ethylene oxide) Electrolytes: A New Approach for Practical Lithium-Metal Polymer Batteries. *J. Am. Chem. Soc.* **2014**, *136*, 7395−7402.

(17) Monroe, C.; Newman, J. The Impact of Elastic Deformation on Deposition Kinetics at Lithium/Polymer Interfaces. *J. Electrochem. Soc.* **2005**, *152*, A396−A404.

(18) Sharafi, A.; Meyer, H. M.; Nanda, J.; Wolfenstine, J.; Sakamoto, J. Characterizing the Li−$Li_7La_3Zr_2O_{12}$ interface stability and kinetics as a function of temperature and current density. *J. Power Sources* **2016**, *302*, 135−139.

(19) Cheng, L.; Park, J. S.; Hou, H.; Zorba, V.; Chen, G.; Richardson, T.; Cabana, J.; Russo, R.; Doeff, M. Effect of microstructure and surface impurity segregation on the electrical and electrochemical properties of dense Al-substituted $Li_7La_3Zr_2O_{12}$. *J. Mater. Chem. A* **2014**, *2*, 172−181.
(20) Sharafi, A.; Kazyak, E.; Davis, A. L.; Yu, S.; Thompson, T.; Siegel, D. J.; Dasgupta, N. P.; Sakamoto, J. Surface Chemistry Mechanism of Ultra-Low Interfacial Resistance in the Solid-State Electrolyte $Li_7La_3Zr_2O_{12}$. *Chem. Mater.* **2017**, *29*, 7961−7968.
(21) Baek, S.-W.; Lee, J.-M.; Kim, T. Y.; Song, M.-S.; Park, Y. Garnet related lithium ion conductor processed by spark plasma sintering for all solid state batteries. *J. Power Sources* **2014**, *249*, 197−206.
(22) Gao, Z.; Sun, H.; Fu, L.; Ye, F.; Zhang, Y.; Luo, W.; Huang, Y. Promises, Challenges, and Recent Progress of Inorganic Solid-State Electrolytes for All-Solid-State Lithium Batteries. *Adv. Mater.* **2018**, *30*, 1705702.
(23) Kotobuki, M.; Kanamura, K.; Sato, Y.; Yoshida, T. Fabrication of all-solid-state lithium battery with lithium metal anode using Al_2O_3-added $Li_7La_3Zr_2O_{12}$ solid electrolyte. *J. Power Sources* **2011**, *196*, 7750−7754.
(24) Larraz, G.; Orera, A.; Sanjuán, M. L. Cubic phases of garnet-type $Li_7La_3Zr_2O_{12}$: the role of hydration. *J. Mater. Chem. A* **2013**, *1*, 11419−11428.
(25) Kim, K. M.; Shin, D. O.; Lee, Y.-G. Effects of preparation conditions on the ionic conductivity of hydrothermally synthesized Li_{1+x} $Al_xTi_{2-x}(PO_4)_3$ solid electrolytes. *Electrochim. Acta* **2015**, *176*, 1364−1373.
(26) Lin, X.; Wang, H.; Du, H.; Xiong, X.; Qu, B.; Guo, Z.; Chu, D. Growth of Lithium Lanthanum Titanate Nanosheets and Their Application in Lithium-Ion Batteries. *ACS Appl. Mater. Interfaces* **2016**, *8*, 1486−1492.
(27) Jin, Y.; McGinn, P. J. Bulk solid state rechargeable lithium ion battery fabrication with Al-doped $Li_7La_3Zr_2O_{12}$ electrolyte and $Cu_{0.1}V_2O_5$ cathode. *Electrochim. Acta* **2013**, *89*, 407−412.
(28) Han, X.; Gong, Y.; Fu, K.; He, X.; Hitz, G. T.; Dai, J.; Pearse, A.; Liu, B.; Wang, H.; Rubloff, G.; Mo, V.; Wachsman, E. D.; Hu, L. Negating interfacial impedance in garnet-based solid-state Li metal batteries. *Nat. Mater.* **2017**, *16*, 572.
(29) Fu, K.; Gong, Y.; Liu, B.; Zhu, Y.; Xu, S.; Yao, Y.; Luo, W.; Wang, C.; Lacey, S. D.; Dai, J.; Chen, Y.; Wachsman, E.; Hu, L. Toward garnet electrolyte-based Li metal batteries: An ultrathin, highly effective, artificial solid-state electrolyte/metallic Li interface. *Sci. Adv.* **2017**, *3*, No. e1601659.
(30) Zhang, X.; Liu, T.; Zhang, S.; Huang, X.; Xu, B.; Lin, Y.; Xu, B.; Li, L.; Nan, C.-W.; Shen, Y. Synergistic Coupling between $Li_{6.75}La_3Zr_{1.75}Ta_{0.25}O_{12}$ and Poly(vinylidene fluoride) Induces High Ionic Conductivity, Mechanical Strength, and Thermal Stability of Solid Composite Electrolytes. *J. Am. Chem. Soc.* **2017**, *139*, 13779−13785.
(31) Rosero-Navarro, N. C.; Tadanaga, K. *Handbook of Sol-Gel Science and Technology: Processing, Characterization and Applications*; Springer, 2018; pp 2631−2648.
(32) Li, C.; Liu, Y.; He, J.; Brinkman, K. S. Ga-substituted $Li_7La_3Zr_2O_{12}$: An investigation based on grain coarsening in garnet-type lithium ion conductors. *J. Alloys Compd.* **2017**, *695*, 3744−3752.
(33) Joseph, J.; Murdock, A. T.; Seo, D. H.; Han, Z. J.; O'Mullane, A. P.; Ostrikov, K. K. Plasma Enabled Synthesis and Processing of Materials for Lithium-Ion Batteries. *Adv. Mater. Technol.* **2018**, *3*, 1800070.
(34) Lü, X.; Howard, J. W.; Chen, A.; Zhu, J.; Li, S.; Wu, G.; Dowden, P.; Xu, H.; Zhao, Y.; Jia, Q. Antiperovskite Li_3OCl Superionic Conductor Films for Solid-State Li-Ion Batteries. *Adv. Sci.* **2016**, *3*, 1500359.
(35) Oudenhoven, J. F. M.; Baggetto, L.; Notten, P. H. L. All-Solid-State Lithium-Ion Microbatteries: A Review of Various Three-Dimensional Concepts. *Adv. Energy Mater.* **2011**, *1*, 10−33.
(36) Liu, W.; Lee, S. W.; Lin, D.; Shi, F.; Wang, S.; Sendek, A. D.; Cui, Y. Enhancing ionic conductivity in composite polymer electrolytes with well-aligned ceramic nanowires. *Nat. Energy* **2017**, *2*, 17035.
(37) Fu, K.; Gong, Y.; Dai, J.; Gong, A.; Han, X.; Yao, Y.; Wang, C.; Wang, Y.; Chen, Y.; Yan, C.; Li, E. D.; Hu, L. Flexible, solid-state, ion-conducting membrane with 3D garnet nanofiber networks for lithium batteries. *Proc. Natl. Acad. Sci. U.S.A.* **2016**, *113*, 7094−7099.
(38) Medeiros, E. S.; Glenn, G. M.; Klamczynski, A. P.; Orts, W. J.; Mattoso, L. H. C. Solution blow spinning: A new method to produce micro- and nanofibers from polymer solutions. *J. Appl. Polym. Sci.* **2009**, *113*, 2322−2330.
(39) Sinha-Ray, S.; Yarin, A. L.; Pourdeyhimi, B. The production of 100/400 nm inner/outer diameter carbon tubes by solution blowing and carbonization of core−shell nanofibers. *Carbon* **2010**, *48*, 3575−3578.
(40) Sinha-Ray, S.; Zhang, Y.; Yarin, A. L.; Davis, S. C.; Pourdeyhimi, B. Solution Blowing of Soy Protein Fibers. *Biomacromolecules* **2011**, *12*, 2357−2363.
(41) Yarin, A. L.; Pourdeyhimi, B.; Ramakrishna, S. *Fundamentals and Applications of Micro-and Nanofibers*; Cambridge University Press: 2014.
(42) Kolbasov, A.; Sinha-Ray, S.; Joijode, A.; Hassan, M. A.; Brown, D.; Maze, B.; Pourdeyhimi, B.; Yarin, A. L. Industrial-Scale Solution Blowing of Soy Protein Nanofibers. *Ind. Eng. Chem. Res.* **2015**, *55*, 323−333.
(43) Benito, J. G.; Teno, J.; Torres, D.; Díaz, M. Solution Blow Spinning and Obtaining Submicrometric Fibers of Different Polymers. *Int. J. Nanoparticles Nanotechnol.* **2017**, *3*, 1.
(44) Daristotle, J. L.; Behrens, A. M.; Sandler, A. D.; Kofinas, P. A Review of the Fundamental Principles and Applications of Solution Blow Spinning. *ACS Appl. Mater. Interfaces* **2016**, *8*, 34951−34963.
(45) Li, J.; Song, G.; Yu, J.; Wang, Y.; Zhu, J.; Hu, Z. Preparation of Solution Blown Polyamic Acid Nanofibers and Their Imidization into Polyimide Nanofiber Mats. *Nanomaterials* **2017**, *7*, 395.
(46) Yarin, A. L.; Lee, M. W.; An, S.; Yoon, S. S. *Self-Healing Nanotextured Vascular Engineering Materials*; Springer Nature Switzerland AG, 2019.
(47) Sinha-Ray, S.; Srikar, R.; Lee, C. C.; Li, A.; Yarin, A. L. Shear and Elongational Rheology of Gypsum Slurries. *Appl. Rheol.* **2011**, *21*, 63071.
(48) Gao, X.; Fisher, C. A. J.; Kimura, T.; Ikuhara, Y. H.; Kuwabara, A.; Moriwake, H.; Oki, H.; Tojigamori, T.; Kohama, K.; Ikuhara, Y. Domain boundary structures in lanthanum lithium titanates. *J. Mater. Chem. A* **2014**, *2*, 843−852.
(49) Ma, C.; Cheng, Y.; Chen, K.; Li, J.; Sumpter, B. G.; Nan, C.-W.; More, K. L.; Dudney, N. J.; Chi, M. Mesoscopic Framework Enables Facile Ionic Transport in Solid Electrolytes for Li Batteries. *Adv. Energy Mater.* **2016**, *6*, 1600053.
(50) Yuan, Y.; Amine, K.; Lu, J.; Shahbazian-Yassar, R. Understanding materials challenges for rechargeable ion batteries with in situ transmission electron microscopy. *Nat. Commun.* **2017**, *8*, 15806.
(51) Yeon, S.-H.; Kim, K.-S.; Choi, S.; Cha, J.-H.; Lee, H. Characterization of PVdF(HFP) Gel Electrolytes Based on 1-(2-Hydroxyethyl)-3-methyl Imidazolium Ionic Liquids. *J. Phys. Chem. B* **2005**, *109*, 17928−17935.
(52) Reznik, S. N.; Yarin, A. L.; Zussman, E.; Bercovici, L. Evolution of a compound droplet attached to a core-shell nozzle under the action of a strong electric field. *Phys. Fluids* **2006**, *18*, 062101.

https://dx.doi.org/10.1021/acsami.9b19851
ACS Appl. Mater. Interfaces 2020, 12, 16200−16208